

1 **The outflow of Asian biomass burning carbonaceous aerosol into the UTLS in spring:**
2 **Radiative effects seen in a global model**

3 Prashant Chavan^{1,2}, Suvarna Fadnavis^{1*}, Tanusri Chakroborty¹, Christopher E. Sioris³, Sabine
4 Griessbach⁴, Rolf Müller⁵

5 ¹Indian Institute of Tropical Meteorology, Center for climate change, MoES, India

6 ²Savitribai Phule Pune University, Pune, India,

7 ³Air Quality Research Division, Environment and Climate Change, Toronto, Canada

8 ⁴Forschungszentrum Jülich GmbH, Jülich Supercomputing Center, Jülich, Germany,

9 ⁵Forschungszentrum Jülich GmbH, IEK7, Jülich, Germany

10 Corresponding author email: suvarna@tropmet.res.in

11 **Abstract**

12 Biomass burning (BB) over Asia is a strong source of carbonaceous aerosols during spring.
13 From ECHAM6-HAMMOZ model simulations and satellite observations, we show that there
14 is an outflow of Asian BB carbonaceous aerosols into the Upper Troposphere and Lower
15 Stratosphere (UTLS) (black carbon: 0.1 to 6 ng m⁻³ and organic carbon: 0.2 to 10 ng m⁻³)
16 during the spring season. The model simulations show that the greatest transport of BB
17 carbonaceous aerosols into the UTLS occurs from the Indochina and East Asia region by
18 deep convection over the Malay peninsula and Indonesia. The increase in BB carbonaceous
19 aerosols enhances atmospheric heating by 0.001 to 0.02 K day⁻¹ in the UTLS. The aerosol-
20 induced heating and circulation changes increase the water vapour mixing ratios in the upper
21 troposphere (by 20-80 ppmv) and in the lowermost stratosphere (by 0.02-0.3 ppmv) over the
22 tropics. Once in the lower stratosphere, water vapour is further transported to the South Pole
23 by the lowermost branch of the Brewer-Dobson circulation. These aerosols enhance the in-
24 atmosphere radiative forcing (0.68±0.25 W m⁻² to 5.30±0.37 W m⁻²), exacerbating
25 atmospheric warming but produce a cooling effect on climate (TOA: -2.38±0.12 W m⁻² to -
26 7.08±0.72 W m⁻²). The model simulations also show that Asian carbonaceous aerosols are
27 transported to the Arctic in the troposphere. The maximum enhancement in aerosol extinction
28 is seen at 400 hPa (by 0.0093 km⁻¹) and associated heating rates at 300 hPa (by 0.032 K day⁻¹
29 ¹) in the Arctic.

30 1. Introduction

31

32 There is growing concern about increasing aerosol amounts over South and East Asia,
33 not only because of its contribution to air pollution and its harmful health effects (Chen et al.,
34 2017; Thomas et al., 2019), but also because of its impact on the hydrological cycle (Meehl et
35 al., 2008). Biomass burning (BB) accounts for ~60% of the total aerosol optical depth (AOD)
36 globally (Cheng et al., 2009; Streets et al., 2003). It is one of the major sources of large
37 carbonaceous aerosol (Ni et al., 2019). BB is responsible for the major fraction of global
38 mean emissions of black carbon (BC, ~59%) and organic carbon (OC, ~85%) (Bond et al.,
39 2013).

40

41 In Asia, China (25%) is the largest contributor to the global BB aerosol emissions,
42 followed by India (18%), Indonesia (13%), and Myanmar (8%) (Streets et al., 2003). Among
43 the sources, forest burning (anthropogenic and natural) contributes 45%, burning of crop
44 residues in the field 35%, and burning grassland and savannah 20% to the total BB aerosols
45 in Asia (Streets et al., 2003). Asia emits a substantial amount of BC ($\sim 0.45 \text{ Tg yr}^{-1}$) and OC
46 ($\sim 3.3 \text{ Tg yr}^{-1}$) from BB (Streets et al., 2003). These are significant fractions of the global BB
47 emissions of BC ($\sim 2.8\text{--}4.9 \text{ Tg yr}^{-1}$) and OC ($\sim 31\text{--}36 \text{ Tg yr}^{-1}$), respectively (Andreae, 2019).
48 Recently, Wu et al. (2018) and Singh et al. (2020) reported ~83% of the carbonaceous aerosol
49 mass is emitted from open fires over South and East Asia. Within Asia, BB carbonaceous
50 aerosol emissions from East Asia (BC: 110 Gg, OC: 730 Gg) are larger than over India (BC:
51 83 Gg, OC: 650 Gg) and the Indochina region (BC: 40 Gg, OC: 310 Gg) (Streets et al.,
52 2003).

53

54 Biomass burning over Asia shows a strong seasonal cycle peaking in spring (Streets et
55 al., 2003). Our analysis of MODIS fire counts over Asia also shows a pronounced peak in
56 spring (Fig. 1a). The carbonaceous aerosols emitted from BB also peak in spring over
57 Indochina, South Asia, and East Asia regions (Fig. 1b). These aerosols will affect the regional
58 radiative forcing. The literature shows that aerosols emitted from BB in spring produce a
59 significant negative radiative forcing at the top of the atmosphere (TOA) and at the surface,
60 but in-atmospheric radiative forcing (TOA - surface) is positive over Asia (Wang et al., 2007;
61 Lin et al., 2014; Singh et al., 2020).

62

63 Deep convection occurs over the Bay of Bengal, the South China Sea, and Malay
64 Peninsula during the spring and monsoon seasons (Randel et al., 2010; Fadnavis et al., 2013;
65 Murugavel et al., 2012) that may transport Asian boundary layer pollutants to the UTLS.
66 Numerous airborne measurements show evidence of carbonaceous aerosol in the upper
67 troposphere over Asia and adjoining outflow regions during spring and monsoon seasons,
68 e.g., measurements from the Civil Aircraft for Regular Investigation of the Atmosphere Based
69 on an Instrument Container (CARIBIC) campaign in 2004, Stratospheric and upper
70 tropospheric processes for better climate predictions (StratoClim) in 2017, Aerosol Radiative
71 Forcing in East Asia (A-FORCE) in 2009, and Transport and Chemical Evolution over the
72 Pacific (TRACE-P) in 2001 (Nguyen et al., 2008; Pozzoli et al., 2008; Oshima et al., 2012;
73 Weigel et al., 2020; Brunamonti et al., 2018; Hanumanthu et al., 2020). There may be a
74 significant contribution from BB to the observed carbonaceous aerosols in the UTLS, since
75 BB accounts for ~59 - 80 % of the carbonaceous aerosols globally (Bond et al., 2013) and
76 being fine-grained, these aerosols have long atmospheric residence times. Transport of
77 Australian wildfire smoke into the stratosphere (~35km) is seen in satellite observations
78 (Khaykin et al., 2020). The balloon-borne, lidar, and satellite observations showed pyro-

79 cumulonimbus events that injected smoke from Canadian forest fires into the stratosphere in
80 August 2017 (Peterson et al., 2018; Hooghiem et al., 2020; Lestrelin et al., 2021). The
81 carbonaceous aerosols were transported to the upper troposphere and produced significant
82 heating locally (Fadnavis et al., 2017a). The heating of the upper troposphere induces an
83 amplification of the vertical motion in the troposphere (Fadnavis et al., 2017b; Hooghiem, et
84 al., 2020).

85

86 Numerous studies show the transport of boundary layer aerosols from Asia to the
87 lower stratosphere during the monsoon season (Randel et al., 2010; Fadnavis et al., 2013).
88 However, transport of Asian aerosol pollution into the UTLS during the spring season is not
89 reported hitherto when the deep convection occurs over the Malay peninsula (Chang et al.,
90 2005) and Indonesia, and when biomass burning aerosol emissions show a peak (Streets et
91 al., 2003; Fig. 1). In this study, we address these unexplored science questions (1) transport
92 pathways of Asian BB aerosols to the lower stratosphere during the spring season, (2)
93 impacts of Asian BB carbonaceous aerosols on the lower stratosphere. For this purpose, we
94 employ the state-of-the-art ECHAM6-HAMMOZ chemistry-climate model. The model is
95 evaluated against satellite (MODIS) and ground-based remote sensing (AERONET). The
96 paper is organized as follows: satellite data, ground-based data and the experimental set-up
97 are described in section 2. Section 3 comprises a discussion on the distribution of fires and
98 model evaluation; results are discussed in section 4; conclusions are given in section 5.

99

100

101

102

103

104 2. Model simulations and satellite observations

105 2.1 Model description and experimental set-up

106

107 The fully coupled chemistry-climate model ECHAM6.3–HAM2.3 is used in this study.
108 It comprises the general circulation model ECHAM6 coupled to the aerosol sub-module
109 “Hamburg Aerosol Model (HAM)” (Stier et al., 2005). HAM predicts the evolution of sulfate
110 (SU), BC, OC, particulate organic matter (POM), sea salt (SS), and mineral dust (DU)
111 aerosols. The size distribution of the aerosol population is described by seven lognormal
112 modes with prescribed variance in the aerosol module (Stier et al., 2005). [The anthropogenic
113 and fire emissions were obtained from the ACCMIP-II \(Emissions for Atmospheric
114 Chemistry and Climate Model Intercomparison Project\) emission inventories and are
115 interpolated for the period 2000 - 2100 by using Representative Concentration Pathway 4.5
116 \(RCP4.5\) \(Lamarque et al., 2010; van Vuuren et al., 2011\). The biomass burning emissions
117 dataset represent average conditions of the decade \(Tegen et al., 2019\). It should be noted that
118 inter-annual variability of biomass burning is not considered in our simulations. Injection
119 heights of biomass burning emissions are documented by Val Martin et al. \(2010\). The
120 majority \(75%\) of the emissions are evenly distributed within the planetary boundary layer
121 \(PBL\) with 17% in the first \[model level above the planetary boundary layer\]\(#\) and 8% in the
122 second \[model level above the planetary boundary layer\]\(#\) \(Tegen et al., 2019\). Biogenic
123 emissions are derived from MEGAN \(Guenther 1995\). In the model, biogenic OC is directly
124 inserted via emissions. Secondary organic aerosol \(SOA\) emissions are as described by
125 Dentener et al. \(2006\).](#)

126

127 The model simulations are performed at a T63 spectral resolution corresponding to
128 $1.875^\circ \times 1.875^\circ$ horizontal resolution, while 47 hybrid σ -p levels provide the vertical

129 resolution from the surface up to 0.01 hPa. The model has 12 vertical levels in the UTLS
130 (300 to 50 hPa). The simulations have been carried out at a time step of 20 min. Atmospheric
131 Model Inter-comparison Project (AMIP) [monthly varying](#) sea surface temperature (SST) and
132 sea ice cover (SIC) were used as lower boundary conditions. [We performed two sets of](#)
133 [emission sensitivity experiments; in one set of the simulations, the aerosol emissions from](#)
134 [biomass burning were kept on \(referred to as BMaeroon simulations\) and in another set of the](#)
135 [simulations, the aerosol emissions from biomass burning were kept off \(referred to as](#)
136 [BMaerooff simulations\).](#) We adopted an ensemble mean approach (with ten ensemble
137 members) for the above two experiments. Ten spin-up simulations were performed from 1-10
138 January 2012 up to 28 February 2013 to generate stabilized initial fields for the ten ensemble
139 members. Emissions were the same in each of the ten members during the spin-up period. In
140 the BMaerooff simulations (ten ensemble members each), the biomass burning aerosols were
141 switched off since 1 March 2013. The BMaeroon and BMaerooff simulations ended on 31
142 December 2013. To investigate the effects of biomass burning aerosol emissions in spring
143 (i.e., since 1 March 2013), we analyze the difference between BMaeroon and BMaerooff
144 simulations for the spring season in 2013. The uncertainty estimates in simulated radiative
145 forcing, heating rates, aerosol extinction coefficient are obtained from the 10 members of the
146 different initial conditions. The year 2013 was chosen for the analysis as this was a neutral
147 year without a pronounced El Niño or Indian Ocean Dipole oscillation. [Such large-scale](#)
148 [coupled atmosphere–ocean oscillations substantially affect the transport processes to the](#)
149 [UTLS \(Fadnavis et al., 2017a, 2019\).](#)

150

151

152

153

154 2.2 MODIS fire counts and aerosol optical depth

155

156 In order to study spatio-temporal variations in the biomass burning activity, we analysed the
157 Terra/Aqua combined daily active fire location data (product mcd14dl) from the Moderate
158 Resolution Imaging Spectroradiometer (MODIS)
159 (<https://firms.modaps.eosdis.nasa.gov/download/>) onboard Terra and Aqua (Earth Observing
160 System). This MODIS collection-6, Level-2 global data are processed by NASA's Land,
161 Atmosphere Near real-time Capability for EOS (LANCE) Fire Information for Resource
162 Management System (FIRMS), using swath products (MOD14/MYD14). The thermal
163 anomaly / active fire represents the centre of a 1 km pixel that is flagged by the MODIS
164 MOD14/MYD14 Fire and Thermal Anomalies algorithm as containing one or more fires
165 within the pixel (Giglio et al., 2003). The fire detection algorithm uses the strong mid-
166 infrared (IR) emissions from the fires (Matson and Dozier 1981) and is based on the
167 brightness temperatures derived from MODIS at the 4 and 11- μm channels. The retrieval
168 algorithm classifies fire pixels in three categories: low confidence (0 – 30 %), nominal
169 confidence (30 – 80 %), and high confidence (>80 %). This confidence limit allows the
170 rejection of false fires (Giglio, 2015). Here, data with high or nominal confidence (≥ 70 %)
171 are used.

172

173 For information on aerosol, we used monthly mean data from MODIS Terra (MOD08
174 M3 V6.1) at $1^\circ \times 1^\circ$ horizontal resolution to study AOD variability over the Asian region
175 during spring 2013. MODIS Terra measures radiance emanating from the surface and the
176 atmosphere and provides images in 36 spectral bands between 0.415 and 14.235 μm , with a
177 spatial resolution varying from 250 m to 1 km (Mhawish et al., 2019). Terra MODIS

178 MOD08_M3 (V6.1) aerosol products (i.e., AOD) are retrieved using the Deep Blue (DB)
179 algorithm. The algorithm calculates the column aerosol loading at 0.55 μm over land and
180 ocean.

181

182 **2.3 Multi-Angle Imaging Spectroradiometer (MISR), Aerosol Robotic NETwork** 183 **(AERONET) and Optical Spectrograph and InfraRed Imaging System (OSIRIS)** 184 **observations**

185

186 The AOD retrievals from the Multi-Angle Imaging Spectroradiometer (MISR) at 550
187 nm wavelength and the Aerosol Robotic NETwork (AERONET) sunphotometer during
188 spring 2013 are also used for comparison with the model simulations. Details of MISR are
189 available at <https://misr.jpl.nasa.gov/getData/accessData/> and AERONET at
190 <https://aeronet.gsfc.nasa.gov/>. AERONET AOD observations are obtained at different stations
191 in the Indochina region (Myanmar: 16.86°N - 96.15°E, Vientiane: 17.99°N-102.57°E,
192 Siplakorn University: 13.81°N-100.04°E, Ubon-Ratchathani: 15.24°N - 104.87°E), South
193 Asia (Gandhi college: 25.81°N - 85.12°E, Lumbini: 27.49°N-83.28°E, Kathmandu Bode:
194 27.68°N -85.39°E, Dhaka University: 23.72°N - 90.39°E), East Asia (Nghia-Do: 21.04°N -
195 105.80°E, Hong Kong Polytechnic University: 22.30°N - 114.18°E).

196

197 We compared simulated aerosol extinction coefficient vertical profiles with
198 observations from Optical Spectrograph and InfraRed Imaging System (OSIRIS) on-board
199 the Odin satellite (Bourassa et al., 2012). We used version 7.0 vertical profiles of aerosol
200 extinction at 750 nm for March-May 2013 ([https://research-groups.usask.ca/osiris/data-](https://research-groups.usask.ca/osiris/data-products.php#Download)
201 [products.php#Download](https://research-groups.usask.ca/osiris/data-products.php#Download)). The limb scatter measurements from OSIRIS show good
202 agreement with Stratospheric Aerosol and Gas Experiment (SAGE) II and Scanning Imaging

203 Absorption spectrometer for Atmospheric Chartography (Rieger et al., 2018). To understand
204 convective activity in spring 2013, we also analyzed Outgoing Longwave Radiation (OLR)
205 data for March - May 2013 from the National Center for Environmental Prediction (NCEP)
206 re-analysis-2 (<https://psl.noaa.gov/data/gridded/data.ncep.reanalysis2.pressure.html>).

207

208 **3. Distribution of fires and model evaluation**

209 **3.1 Seasonal distribution of fires over Asia**

210

211 In this section, we discuss the seasonal variability of fire activity in Asia. The fire
212 counts peak over Asia (10°S - 50°N, 60°E - 130°E) in the spring season. Figure 1a-b shows
213 that fires are clustered over three sub-regions (1) Indochina region (91°E - 107°E, 10°N -
214 27°N) (numbers of fire counts: 80694), (2) East Asia (108°E - 123°E, 22°N - 32°N),
215 (numbers of fire counts: 4770), (3) South Asia (65°E - 90°E, 8°N - 32°N) (numbers of fire
216 counts: 14223) (Fig. 1b). Fire counts over the three sub-regions peak in spring although the
217 month varies, e.g., fire counts over East Asia show a peak in March, Indochina region in
218 March-April, and South Asia in May (Fig. 1a). The fire counts over South Asia show a
219 secondary peak in October. In agreement with our results, Bhardwaj et al. (2016) also
220 reported high fire activity in spring and the lowest fire activity during the monsoon (June–
221 September) in the 2003-2013 time frame. Streets et al. (2003) reported that higher fire counts
222 during the spring season over South Asia and East Asia are attributed to enhanced crop
223 burning activity. Over the Indochina region, high fire counts are associated with forest fires
224 along with crop burning. Intense biomass burning activity over Asia during the spring season
225 is also reported by Zhang et al. (2020). Hence, we provide further analysis in spring.

226

227

228 3.2. Model evaluation

229

230 We compare simulated AOD (averaged for spring from BMAeroon simulations) with
231 MODIS, MISR, and AERONET. Figure 2 (a-c) shows large AOD over the regions: Indochina
232 (MODIS: ~0.4 to 0.8, MISR: 0.27 to 0.6; model: 0.27 to 0.5), East Asia (MODIS: 0.5 to 1.3,
233 MISR: 0.27 to 1, model: 0.5 to 1.4), and the Indo-Gangetic plain in south Asia (23°N -30°N,
234 75°E - 85°E) (MODIS: 0.24 to 0.8, MISR: 0.24 to 0.5, model: 0.3 to 0.6). The MISR AOD is
235 comparatively less than MODIS AOD over all three study regions (Fig. 2a-b). There are
236 differences in the spatial distribution of AOD among MODIS, MISR and the model. Over
237 East Asia, the model overestimates AOD relative to MISR (by 0.24) and MODIS (by 0.1).
238 Over Indochina, the model shows an underestimation compared to MISR (by 0.1) and
239 MODIS (by 0.2). The simulated AOD is over-estimated over the Indo-Gangetic plain in
240 comparison with MISR (by 0.08) and underestimated compared to MODIS (0.2). The
241 simulated AOD is underestimated south of 13°N compared to MISR and MODIS (MODIS:
242 0.4 to 0.7, MISR:0.4 to 0.6, model: 0.21 to 0.3) and overestimated over central India (lat: 20°
243 - 28°N lon: 75°E - 88°E) compared to MODIS and MISR (MODIS:0.16 to 0.4, MISR:0.21 to
244 0.3, model: 0.3 to 0.5). These issues may be due to a higher amount of dust emission in the
245 model over West Asia that is transported to India. In the past, a number of papers reported
246 that transport of dust occurs from west Asia to the Indo-Gangetic plain and the Tibetan
247 Plateau region during spring (Lau and Kim 2006; Fadnavis et al., 2017b, Fadnavis et al.,
248 2021a). Simulated AOD is also overestimated over the Tibetan Plateau and East Asian region
249 (MODIS: 0.21 to 1.0, MISR: 0.16 to 0.6, model: 0.27 to 1.2). The distribution of dust AOD
250 also shows high amounts over these regions (See Fig. S1). This indicates that higher amounts
251 of dust over the Tibetan Plateau and the East Asia region cause overestimation of AOD there.
252 Tegen et al. (2019) also reported that in ECHAM6–HAMMOZ simulations the AOD is

253 overestimated over East Asia in comparison with MISR. The model simulations
254 underestimate the AOD over the Himalayas in comparison with MODIS (MODIS: 0.24 to
255 0.3, MISR: 0.1 to 0.21, model: 0.1 to 0.3). It should be noted that dust
256 emission/parameterization is the same in both BMaeroon and BMaerooff simulations.

257

258 Further, we compare simulated AOD with ground-based measurements at ten
259 AERONET stations during spring 2013 (Figure 2d). Model results were sampled at each
260 station at the same time. Comparison with AERONET observations also shows that the model
261 underestimates AOD over all the stations. The simulated AOD (0.54) shows the highest
262 underestimation at Nghia Do (21.04°N - 105.80°E) in East Asia and the lowest
263 underestimation at Gandhi college (25.81°N - 85.12°E) in the Indo-Gangetic plain, where the
264 simulated 550 nm AOD is 0.57.

265

266 The differences in the magnitude of AOD between model, satellite remote sensing
267 (MISR, MODIS), and ground-based AERONET observations may be caused by various
268 factors; e.g., satellite remote sensing of AOD exhibits biases over certain surface types. The
269 differences between MISR and MODIS may be due to differences in their calibration,
270 algorithm assumptions, or the aerosol models in the lookup tables used in the retrieval
271 algorithms (Addou et al., 2005; Choi et al., 2019). There are uncertainties in the model
272 emission inventories (Fadnavis et al., 2013, 2017, 2019).

273

274 The vertical distribution of simulated aerosol extinction coefficient profiles
275 (BMaeroon) averaged over the BB burning region (10°N - 30°N) are compared with OSIRIS
276 observations in spring 2013 (Fig. 2e-f). Our model could simulate vertical variations similar
277 to those observed by OSIRIS. A plume rising from 90°E - 120°E extends to 16 km is also

278 evident in the OSIRIS data although the model underestimates the aerosol extinction
279 coefficient by 0.0002 - 0.0003 km⁻¹. The sign of the difference is consistent with the slightly
280 shorter wavelength of the OSIRIS extinction measurements. This underestimation may also
281 be due to uncertainties in the model due to emission inventory and transport processes in the
282 model. It should be noted that there may be biases in OSIRIS measurements due to
283 assumptions made on the aerosol size distribution and chemical composition (Bourassa et al.,
284 2012).

285

286 **4. Results**

287 **4.1 Impact of biomass burning on Aerosol Optical Depth (AOD)**

288

289 Figure 3 (a) shows the distribution of anomalies in simulated AOD (BMAeroon-
290 BMAerooff). It shows enhanced AOD anomalies over the Indo-Gangetic plain (~0.22 to 0.8),
291 the Tibetan Plateau and the north eastern parts of East Asia (~0.3 to 1.2). The distribution of
292 anomalies in dust AOD shows high amounts over these regions. It indicates that dust
293 enhancement over the Indo-Gangetic plain (~0.22 to 0.8), the Tibetan Plateau and the
294 northeastern parts of East Asia (0.8 to 1) (Fig. 3b) causes enhancement in AOD there. The
295 simulated dust anomalies and circulation patterns also show transport of enhanced dust from
296 West Asia to North India and the Indo-Gangetic plain region in the lower troposphere (Fig. 3b
297 and Fig. S2a). Dust is also transported from Tibetan Plateau-East Asia region to North India
298 in the mid/upper troposphere (Fig. S2b). The enhanced dust transport from west Asia and
299 Tibetan Plateau-East Asia region to South Asia is induced by atmospheric heating generated
300 by biomass burning carbonaceous aerosols (discussed in section 4.4). This atmospheric
301 heating leads to enhanced dust emission over the respective desert regions. Dust being
302 absorptive in nature contributes to a further increase of the atmospheric heating. The heating

303 led to a formation of a low pressure zone over East India in the lower troposphere (900 hPa)
304 (Fig. 3b) and the Bay of Bengal and Myanmar in the mid-troposphere (500 hPa) (Fig. S2b
305 and Fig. 7b). These circulation changes further enhanced the dust transport from west Asia
306 and the Tibetan Plateau-East Asia region to South Asia.

307

308 Figure 3c shows the spatial distribution of the AOD for carbonaceous aerosols
309 (BC+OC). The changes in concentration of total column carbonaceous aerosols are shown in
310 Fig. S3a. Figures 3c and S3a show increases in aerosols over Indochina (AOD: +0.04-0.07,
311 concentration: +40-80%), Indo-Gangetic plain (AOD: +0.014-0.03, concentration: +10-50%)
312 and East Asia (AOD: +0.018-0.04, concentration: +20-60%). It is evident that anomalies of
313 carbonaceous aerosols AOD over the Indo-Gangetic plain and East Asia are comparatively
314 lower than over the Indochina region. In agreement with our results, Wang et al. (2015) also
315 reported an abundant mixture of BC and OC particles due to BB over the Indochina region in
316 spring 2014. Our model simulations show that the contribution of BB-emitted OC to AOD
317 (Indochina 16 to 35 %; East Asia: 4 to 12 %; South Asia: 0.8 to 4 %) is higher than that of
318 BB-emitted BC (Indochina: 1.8 to 6 %; East Asia: 0.8 to 1.4 %; South Asia: 0.2 to 0.8 %)
319 (Fig. S3b-c). Figure 3c also shows high amounts of carbonaceous aerosols over the western
320 Pacific, which may be due to transport from the Indochina region by westerly winds
321 (discussed later in subsection 4.3).

322

323 **4.2. Impact of BB carbonaceous aerosol on radiative forcing**

324

325 The carbonaceous aerosols emitted from biomass burning may significantly change
326 radiative forcing by absorption and attenuation of solar and terrestrial radiation (Schill et al.,
327 2020). The anomalies (averaged for spring) in net radiative forcing show negative radiative

328 forcing at the surface and top of the atmosphere (TOA) over South Asia (surface: -5.08 ± 0.44
329 W m^{-2} ; TOA: $-4.39 \pm 0.26 \text{ W m}^{-2}$), Indochina region (surface: $-7.68 \pm 0.45 \text{ W m}^{-2}$; TOA: -
330 $2.38 \pm 0.12 \text{ W m}^{-2}$) and East Asia (surface: $-10.81 \pm 0.63 \text{ W m}^{-2}$; TOA: $-7.08 \pm 0.74 \text{ W m}^{-2}$) (Fig.
331 4). The estimates of in-atmosphere radiative forcing show positive anomalies over south Asia
332 ($0.68 \pm 0.25 \text{ W m}^{-2}$), Indochina region ($5.30 \pm 0.37 \text{ W m}^{-2}$), and East Asia ($3.73 \pm 0.20 \text{ W m}^{-2}$),
333 indicating an atmospheric warming. In agreement with our study, a number of studies showed
334 a negative radiative impact at the TOA and surface, but positive in-atmosphere radiative
335 forcing due to BC and OC aerosols over the Indochina region. For example, Lin et al. (2014)
336 reported a radiative forcing of -4.74 W m^{-2} at the TOA, -26.85 W m^{-2} at the surface, thus
337 $+22.11 \text{ W m}^{-2}$ in-atmosphere. Wang et al. (2007) estimated a radiative forcing of -1.4 to -1.9
338 W m^{-2} at the TOA and -4.5 to -6 W m^{-2} at the surface, yielding $+2.6 \text{ W m}^{-2}$ in-atmosphere
339 during March 2001. Singh et al. (2020) also reported a radiative forcing at the TOA of -1.91
340 W m^{-2} and -42.76 W m^{-2} at the surface and 40.85 W m^{-2} in-atmosphere over Myanmar.

341

342 **4.3. Transport of biomass burning aerosol into the upper troposphere and lower** 343 **stratosphere**

344

345 The stepwise evolution of the Asian summer monsoon begins in spring and contributes a
346 significant amount of rainfall to the total annual precipitation over China (25–40%) and over
347 South Asia (~11-20%) due to deep convection over the Bay of Bengal, Tibetan Plateau and
348 South China Sea (Guhathakurta and Rajeevan, 2008; Li et al., 2016). The distribution of
349 outgoing long-wave radiation (OLR) from NCEP reanalysis data during the spring season
350 confirms that deep convection occurs over the maritime continent that extends to the South
351 China Sea, Bay of Bengal, Malay Peninsula and Indonesia (Fig. 5a). Our model simulation
352 shows a distribution of OLR similar to the observations, although OLR is overestimated in

353 the model (Fig. 5b). Figure 5(c)-(d) shows the combined distribution of Cloud Droplet
354 Number Concentration (CDNC), Ice Crystal Number Concentration (ICNC), and vectors of
355 the resolved circulation, which exhibit a strong upwelling in equatorial Asia (10°N - 20°N,
356 85°E - 140°E, Fig. 5c-d). This upwelling associated with deep convection may transport
357 pollutants from the boundary layer into the UTLS.

358

359 We analyzed the vertical distribution of simulated anomalies (BMAeroon -
360 BMAerooff) of BB carbonaceous aerosols obtained over the high fire emission regions, i.e.,
361 Indochina, South Asia, and East Asia in spring 2013 (Fig. 1b). The simulated distribution of
362 BC aerosols (Fig. 6 a-b) and OC aerosols (Fig. 6c-d) over the Indochina region indicates an
363 aerosol plume extending to the lowermost stratosphere. The ascent resolved in the wind
364 vectors together with the distribution of cloud droplets and cloud ice indicate that the
365 transport of these aerosols from the surface to the lowermost stratosphere occurs due to deep
366 convection over the Malay peninsula and Indonesia (Fig. 5a-b). There is an enhancement of
367 BC aerosol concentration by 0.1 – 2 ng m⁻³ (Fig. 6 a-b) and for OC by 0.2 – 5 ng m⁻³ (Fig. 6
368 c-d) in the UTLS (300 - 90 hPa) over the Indochina region.

369

370 In the troposphere, biomass-burning carbonaceous aerosols are transported to the
371 Arctic (Fig. 6a and Fig. 6c). Some previous studies also show aerosol transport from South
372 Asia and East Asia to the Arctic (Shindell et al., 2008; Fisher et al., 2011). The carbonaceous
373 aerosols are also transported towards the Western Pacific (Fig. 6 b-d and 6 f-h). In the Pacific
374 (140°E - 170°W), these aerosols are lifted to the UTLS. Transport of the aerosols from the
375 Indochina region to the Western Pacific has also been reported in the past (Dong and Fu,
376 2015).

377

378 Further, we show the distribution of BB carbonaceous aerosol over East Asia in
379 Figure 6 e-h. It shows that the plume of BC and OC aerosol crosses the tropopause (BC: 0.2–
380 6 ng m^{-3} and OC: 0.2 to 10 ng m^{-3}). Figures 6e and 6g also show that the aerosol plume from
381 the equatorial region is lifted to the UTLS associated with the Indonesian region ($130^\circ\text{E} -$
382 170°E). Similar to the Indochina region, BC and OC aerosols also show poleward transport
383 to the Arctic and horizontal transport towards the Western Pacific (Figures 6f and 6h). These
384 aerosols are vertically transported in the western Pacific region ($130^\circ\text{E} - 170^\circ\text{E}$). The
385 distribution of anomalies of BC and OC near the tropopause (at 100 hPa) shows outflow of
386 Asian carbonaceous aerosols in the UTLS over equatorial Asia and Western Pacific ($5^\circ\text{S}-$
387 20°N , $70^\circ\text{E} - 180^\circ\text{E}$) (Fig. S4).

388

389 BB in South Asia occurs in central India ($70^\circ\text{E} - 90^\circ\text{E}$, $8^\circ\text{N} - 24^\circ\text{N}$) in spring (Fig. 1 b
390 and Singh et al., 2017). BC and OC emissions over South Asia during the spring season are
391 reported in many studies (Talukdar et al., 2015; Guha et al., 2015). The vertical distribution
392 of anomalies of BC and OC over south Asia shows that positive anomalies of BC and OC
393 aerosols extend from the surface to the upper troposphere (300 hPa) (Fig. S5). CALIPSO
394 derived aerosol profiles in spring 2013 also show plumes reaching up to approximately 7 km
395 (400 hPa) (Singh et al., 2020). Unlike the Indochina region, BB carbonaceous aerosols over
396 Indo-Gangetic plain do not reach the lowermost stratosphere during the spring season.
397 Hence, hereafter we focus our discussion on the transport of BB carbonaceous aerosols and
398 their impacts on the UTLS for Indochina and East Asia.

399

400 Further, we analyze the aerosol enhancement over the Arctic ($65^\circ\text{N} - 85^\circ\text{N}$) due to the
401 transport of Asian biomass burning BC and OC aerosols. The vertical distribution of
402 anomalies of aerosol extinction shows an enhancement of $0-0.0093 \text{ km}^{-1}$ in the Arctic (1000 -

403 100hPa) with a peak at 400 hPa (Fig. 7a). Shindell et al. (2008) also showed seasonally
404 varying transport of South Asian aerosols to the Arctic that maximizes in the spring season.

405

406 **4.4 Impact of BB carbonaceous aerosol on heating rates**

407

408 Carbonaceous aerosols in the atmosphere produce significant heating leading to
409 atmospheric warming (Fadnavis et al., 2017b). We obtained anomalies in heating rates
410 (shortwave + longwave) due to carbonaceous aerosols (BMaeroon - BMaerooff). Figure 7b
411 shows the spatial distribution of anomalies in tropospheric heating rates (averaged from
412 surface to tropopause). It shows that carbonaceous aerosols have induced significant
413 tropospheric heating over the location of dense fires; Indo-China/East Asia (0.02 to 0.12
414 K.day⁻¹). Significant heating is seen namely over the Mongolian desert (0.08 - 0.12 K.day⁻¹).
415 The desert region of west Asia (Pakistan, Afghanistan, Turkistan, Kazakhstan) also shows
416 slight heating (0.02 - 0.04 K.day⁻¹). The heating over the desert regions is associated with
417 enhanced emission of dust, a positive feedback to atmospheric heating induced by the
418 carbonaceous aerosols (section 4.1). Heating is higher over the Mongolian desert than over
419 west Asia due to the vicinity of Mongolia to the location of dense fires.

420

421 Further we show the vertical distribution of heating rates over the Indochina region
422 and East Asia in Figures 8a-d. It shows that enhanced BB carbonaceous aerosols have
423 induced enhanced heating of the atmospheric column along the pathway through which they
424 are transported (Fig. 6a-h). The carbonaceous aerosol emissions over the Indochina region
425 and East Asia produced anomalous heating of ~0.1 to 0.04 K day⁻¹ in the lower troposphere
426 (1000 hPa to 400 hPa) and ~0.008 to 0.001 K day⁻¹ near the tropopause (200 hPa to 80 hPa).
427 Figure 6 a, c, e, g shows that descending winds transport BC and OC aerosols from above the

428 tropopause downward and southward to 20°S. The positive anomalies in heating rates of
429 ~0.001 to 0.004 K day⁻¹ in the upper troposphere at ~200 hPa near 20°S may be due to
430 heating by these aerosols. There may be dynamic changes in response to BB carbonaceous
431 aerosol emission. The transported Asian carbonaceous aerosols and associated dynamical
432 changes in the Arctic enhanced heating rates by 0 - 0.032 K day⁻¹ between 1000 - 100 hPa
433 (Fig. 7a). Also, transport of carbonaceous aerosol to the western Pacific (Fig. 6 b, d, f, h) by
434 the westerly winds has increased heating by 0.008 to 0.04 K day⁻¹ and peaks at 250 hPa (0.04
435 K day⁻¹) over the Central Pacific (170°W - 110°W).

436

437 Figure 8 (a-d) shows positive anomalies in heating rates at the tropopause. Heating in
438 the upper troposphere enhances the vertical motion that may enhance the transport into the
439 lower stratosphere (Gettelman et al., 2004). Carbonaceous aerosols cross the tropopause (0.1
440 to 5 ng m⁻³) and enter the lowermost stratosphere (18°N - 24°N) (Figs. 6 a-h). [The cross](#)
441 [tropopause transport is reinforced by enhanced vertical motion \(Fig. S6a-b\) produced by the](#)
442 [heating generated by the carbonaceous aerosols.](#)

443

444 **4.5 Impact of BB carbonaceous aerosol on water vapor**

445

446 The heating produced by the biomass burning carbonaceous aerosols may affect the
447 distribution of water vapor in the troposphere and stratosphere. Figure 9a-b shows anomalies
448 in water vapor (BMAeroon - BMAerooff) over Indochina and East Asia. An interesting feature
449 seen in Fig. 9a-b is the enhanced transport of water vapor (an anomaly of 0.02 - 0.5 ppmv) to
450 the South Pole through the lower stratosphere from Indochina (91°E - 107°E, 10°N - 27°N)
451 and East Asia (108°E - 123°E, 20°N - 35°N). The tropospheric heating might have caused
452 elevated water vapor injection into the lower-stratosphere. The water vapour in the lower

453 stratosphere is further transported to the South Pole by the lower branch of the Brewer-
454 Dobson circulation. The water vapour reaches the Antarctic within a month indicating fast
455 transport.

456

457 The model simulations show noticeable enhancement of water vapor (0.4 to 1.6
458 ppmv) in the northern tropics near the tropopause (150 hPa) and by 0.2 - 0.7 ppmv in the
459 Arctic lower stratosphere (150 hPa) (Fig. 9c). In the tropical lower stratosphere, it is
460 increased by 0.02 - 0.3 ppmv (Fig. 9d). Water vapor, being a greenhouse gas, amplifies global
461 warming leading to positive feedback (e.g., Riese et al., 2012; Sherwood et al., 2018,
462 Fadnavis et al., 2021b). The strong negative anomalies of OLR (Fig. S6c) induced by
463 carbonaceous aerosols also indicate the positive feedback. Fadnavis et al. (2013) also
464 reported an increase in water vapor in the UTLS in response to the enhancement of aerosols.
465 Stratospheric water vapor plays a significant role in climate change (e.g., Oman et al., 2008;
466 Wang et al., 2020; Xie et al., 2020).

467

468 **5. Conclusions**

469

470 A ten-member ensemble of ECHAM6.3–HAM2.3 simulations for the spring season
471 2013, a neutral year, is analyzed to study the transport of carbonaceous aerosol injected by
472 Asian biomass burning into the UTLS and its associated impacts on radiative forcing, heating
473 rates, and water vapor. To validate the model simulations, we compare simulations with
474 observations from (1) MODIS, (2) MISR, (3) AERONET, (4) OSIRIS during spring 2013.
475 The observational analysis shows reasonable agreement with the model simulations.

476

477 The BB emission increases the aerosol burden (AOD) over the Indochina region by
478 0.14 to 0.22 (carbonaceous aerosol concentration increase of +40-80%), India by 0.22 to 0.38
479 (concentration of carbonaceous aerosol: +10-50%), and East Asia by 0.18 to 0.26
480 (concentration of carbonaceous aerosol: +20-60%). Our analysis shows that deep convection,
481 which occurs over the Malay peninsula and Indonesia, transports carbonaceous aerosols
482 from the boundary layer of the Indochina and East Asia region into the lowermost
483 stratosphere (BC: 0.1 to 6 ng m⁻³ for BC, OC: 0.2 to 10 ng m⁻³). In the UTLS, outflow occurs
484 over equatorial Asia and the Western Pacific (10°S - 20°N, 70°E - 180°E). Carbonaceous
485 aerosols originating from Asian biomass burning are also transported to the Arctic. The
486 maximum enhancement in aerosol extinction (by 0.0093 km⁻¹) is seen at 400 hPa over the
487 Arctic.

488

489 The enhanced carbonaceous BC and OC aerosol emitted from BB produces a negative
490 net radiative forcing at the surface (India: -5.08±0.44 W m⁻², Indochina: -7.68±0.45 W m⁻²,
491 and East Asia: -10.81±0.63 W m⁻²), at the TOA (India: -4.39±0.26 W m⁻², Indochina: -
492 2.38±0.12 W m⁻², and East Asia: -7.08±0.74 W m⁻²) and positive net radiative forcing in the
493 atmosphere (India: 0.68±0.25 W m⁻², Indochina: 5.30±0.37 W m⁻², and East Asia: 3.73±0.20
494 W m⁻²) indicating atmospheric warming, but a cooling of the climate at the surface.

495

496 The changes in BB carbonaceous aerosol induce a warming in the troposphere (0.008
497 – 0.1 K day⁻¹) and in the UTLS (~0.001 to 0.008 K day⁻¹) over Asia. The aerosols transported
498 to the Arctic enhance heating by 0 - 0.032 K day⁻¹, peaking at 300 hPa. The outflow of the
499 aerosols in the UTLS over the western Pacific by the westerly winds has increased heating by
500 0.008 to 0.04 K day⁻¹. The atmospheric heating induced by Asian BB carbonaceous aerosols
501 led to the transport of water vapor into the lower stratosphere (0.02 - 0.3 ppmv) over the

502 tropics. In the lower stratosphere, water vapour is transported to the South Pole by the lower
503 branch of the Brewer-Dobson circulation. Water vapor, being a greenhouse gas, amplifies
504 atmospheric heating, leading to positive feedback (e.g., Riese et al., 2012; Sherwood et al.,
505 2018). Our model simulations also show a positive feedback of dust aerosol on atmospheric
506 heating induced by the enhancement of carbonaceous aerosols.

507

508 Furthermore, our analysis shows that Asian biomass burning carbonaceous aerosols
509 lead to moistening of the troposphere in the northern hemisphere and lowermost stratosphere
510 in the northern tropics and southern hemisphere. An increase in stratospheric water vapour is
511 important as it has an impact on stratospheric temperatures and thus indirectly on
512 stratospheric dynamics (Maycock et al., 2013). The moistening of the stratosphere produces a
513 positive feedback on the climate (Banerjee et al., 2019; Dessler et al., 2013).

514

515 *Acknowledgments:* The authors thank the staff of the High Power Computing Centre (HPC) in
516 IITM, Pune, India, for providing computer resources and the team members of MODIS,
517 MISR, and AERONET for providing data. [Authors are thankful to two anonymous reviewers](#)
518 [for their valuable suggestions.](#)

519

520 **Data availability:** The MODIS fire count data were downloaded from
521 <https://firms.modaps.eosdis.nasa.gov/download>. The AOD data from MODIS Terra can be
522 downloaded from <https://ladsweb.modaps.eosdis.nasa.gov/archive/allData/61/MODATML2/>
523 The AOD data from MISR were obtained from
524 <https://mISR.jpl.nasa.gov/getData/accessData/>. The AERONET data were obtained from
525 <https://aeronet.gsfc.nasa.gov/>. Data of NCEP reanalysis-2 outgoing longwave radiation
526 (OLR) were obtained from
527 <https://psl.noaa.gov/data/gridded/data.ncep.reanalysis2.pressure.html>. The OSIRIS aerosol
528 [extinction coefficient can be downloaded from](#) [https://research-groups.usask.ca/osiris/data-](https://research-groups.usask.ca/osiris/data-products.php#Download)
529 [products.php#Download](#)

530 **Author contributions:** S. F. initiated the idea. P. C. and T. C. performed model analysis. R
531 M., S.G and C.E.S. contributed analysis and study design. C. E. S.and S.G. analyzed OSIRIS
532 data. All authors contributed to the writing and discussions of the manuscript.

533 **Competing Interests:** The authors declare no competing interests.

534 **References:**

- 535 Abdou, W. A., Diner, D. J., Martonchik, J. V., Bruegge, C. J., Kahn, R. A., Gaitley, B. J.,
536 Crean, K. A., Remer, L. A., and B. Holben: Comparison of coincident Multiangle
537 Imaging Spectroradiometer and Moderate Resolution Imaging Spectroradiometer
538 aerosol optical depths over land and ocean scenes containing Aerosol Robotic Network
539 sites, *J. Geophys. Res.*, 110, D10S07, doi:10.1029/2004JD004693, 2005.
- 540 Andreae, M. O.: Emission of trace gases and aerosols from biomass burning – an updated
541 assessment, *Atmos. Chem. Phys.*, 19, 8523–8546, [https://doi.org/10.5194/acp-19-8523-](https://doi.org/10.5194/acp-19-8523-2019)
542 [2019](https://doi.org/10.5194/acp-19-8523-2019), 2019.
- 543 Banerjee A., Chiodo, G., Previdi, M., Ponater, M., Conley, A. J., Polvani L. M.: Stratospheric
544 water vapor: an important climate feedback, *Clim. Dyn.*, 53, 1697–1710,
545 <https://doi.org/10.1007/s00382-019-04721-4>, 2019.
- 546 Bhardwaj, P. M., Naja, R., Kumar, and Chandola, H. C.: Seasonal, interannual, and long-term
547 variabilities in biomass burning activity over South Asia, *Environ. Sci. Pollut. Res.*,
548 23(5), 4397–4410, 2016.
- 549 Bond, T. C., Doherty, S. J., Fahey, D. W., Forster, P. M., Berntsen, T., Deangelo, B. J.,
550 Flanner, M. G., Ghan, S., Kärcher, B., Koch, D., Kinne, S., Kondo, Y., Quinn, P. K.,
551 Sarofim, M. C., Schultz, M. G., Schulz, M., Venkataraman, C., Zhang, H., Zhang, S.,
552 Bellouin, N., Guttikunda, S., K., Hopke P. K., Jacobson, M. Z., Kaiser, J., W., Klimont,
553 Z., Lohmann, U., Schwarz, J. P., Shindell, D., Storelvmo, T., Warren, S. G., and Zender.
554 C. S.: Bounding the role of black carbon in the climate system: A scientific assessment,
555 *J. Geophys. Res. Atmos.* 118(11):5380–5552, 2013.
- 556 Bourassa, A. E., Rieger, L. A., Lloyd, N. D., and Degenstein, D. A.: Odin-OSIRIS
557 stratospheric aerosol data product and SAGE III intercomparison, *Atmos. Chem. Phys.*,
558 12, 605–614, <https://doi.org/10.5194/acp-12-605-2012>, 2012.

559 Brunamonti, S., Jorge, T., Oelsner, P., Hanumanthu, S., Singh, B. B., Ravi Kumar, K.,
560 Sonbawne, S., Meier, S., Singh, D., Wienhold, F.G. , Luo, B.-P., Boettcher, M.,
561 Poltera, Y., Jauhiainen, H., Kayastha, R., Karmacharya, J., Dirksen, R., Naja, M.,
562 Rex, M., Fadnavis, S., and Peter, T.: Balloon-borne measurements of temperature,
563 water vapor, ozone and aerosol backscatter on the southern slopes of the Himalayas
564 during StratoClim 2016–2017, *Atmos. Chem. Phys.*, 18, 15937–15957, 2018,
565 <https://doi.org/10.5194/acp-18-15937-2018>, 2018.

566 Chang, C-P., Wang, Z., McBride, J., and Liu, C-H : Annual Cycle of Southeast Asia—
567 Maritime Continent Rainfall and the Asymmetric Monsoon Transition, *J. Clim.*, 287–
568 301, 18, 2005, <https://doi.org/10.1175/JCLI-3257.1>, 2005.

569 Chen, J. C., Li, Z., Ristovski, A., Milic, Y., Gu, M., S., Islam, S., Wang, J., Hao, H., Zhang,
570 C., He, H., Guo, H., Fu, B., Miljevic, L., Morawska, P., Thai, Y., Fat LAM, G., Pereira,
571 A., Ding, X., Huang, and Dumka. U. C.: A review of biomass burning: Emissions and
572 impacts on air quality, health and climate in China, *Sci. Total Environ.*, 579,1000–1034,
573 2017.

574 Cheng, F. Y., Yang, Z. M., Chang, Y., and Ngan, F.: A numerical study of the dependence of
575 long-range transport of CO to a mountain station in Taiwan on synoptic weather patterns
576 during the Southeast Asia biomass-burning season, *Atmos. Environ.*, 78, 277–90, 2013.

577 Cheng, Y. F., Berghof, M., Garland, R. M., Wiedensohler, A., Wehner, B., Müller, T., Su, H.,
578 Zhang, Y. H., Achtert, P., Nowak, A., Poschl, U., Zhu, T., Hu, M., and Zeng. L. M.:
579 Influence of soot mixing state on aerosol light absorption and single scattering albedo
580 during air mass aging at a polluted regional site in northeastern China, *J. Geophys. Res.*
581 *Atmos.*, 114(11), 1–20, 2009.

582 Choi, M., Lim, H., Kim, J., Lee, S., Thomas T. E., Holben, B. B., Garay, M. J., Hyer, E. E.,
583 Saide, P. P., and Liu, H.: Validation, Comparison, and Integration of GOCI, AHI,

584 MODIS, MISR, and VIIRS Aerosol Optical Depth over East Asia during the 2016
585 KORUS-AQ Campaign, *Atmos. Meas. Tech.* 12 (8): 4619–41.
586 <https://doi.org/10.5194/amt-12-4619-2019>, 2019.

587 Clough, S. A., and Iacono, M. J.: Line-by-line calculation of atmospheric fluxes and cooling
588 rates 2. Application to carbon dioxide, ozone, methane, nitrous oxide and the
589 halocarbons, *J. Geophys. Res.*, 100(D8), 16,519-16,535, 1995.

590 Dentener, F. S., Kinne, T., Bond, O., Boucher, J., Cofala, S., Generoso, P., Ginoux, S., Gong,
591 J., J., Hoelzemann, A., Ito, L., Marelli, J., E., Penner, J., P., Putaud, C., Textor, M.,
592 Schulz, G., R., Van Der Werf, and J., Wilson.: Emissions of primary aerosol and
593 precursor gases in the years 2000 and 1750 prescribed data-sets for AeroCom, *Atmos.*
594 *Chem. and Phys.*, 6(12), 4321–44, 2006.

595 Dessler, A. E., Schoeberl, M. R., Wang, T., Davis, S. M., and Rosenlof, K. H. Stratospheric
596 Water Vapor Feedback, *Proc. Nat. Acad. Sc. U. S.* 110 (45): 18087–91.
597 <https://doi.org/10.1073/pnas.1310344110>, 2013.

598 Dong, X., and Fu, J. S.: Understanding interannual variations of biomass burning from
599 peninsular Southeast Asia, Part II: Variability and different influences in lower and
600 higher atmosphere levels, *Atmos. Environ.*, 115, 9–18, 2015.

601 Fadnavis, S., Chakraborty, T., Ghude S. D., Beig, G., and Raj. P. E.: Modulation of Cyclone
602 Tracks in the Bay of Bengal by QBO, *J. Atmos Terr. Phys.* 73(13):1868–75, 2011.

603 Fadnavis, S., Semeniuk, K., Pozzoli, L., Schultz, M. G., Ghude, S. D., Das, S., and Kakatkar.
604 R.: Transport of Aerosols into the UTLS and Their Impact on the Asian Monsoon
605 Region as Seen in a Global Model Simulation, *Atmos. Chem. and Phys.* 13(17):8771–
606 86. 2013.

607 Fadnavis, S., Kalita, G., Kumar, K. R., Gasparini, B., and Li, J -L. F.: Potential Impact of
608 Carbonaceous Aerosol on the Upper Troposphere and Lower Stratosphere (UTLS) and

609 Precipitation during Asian Summer Monsoon in a Global Model Simulation, *Atmos.*
610 *Chem. and Phys.* 17(18):11637–54, 2017a.

611 Fadnavis S., Roy, C., Sabin, T. P., Ayantika, D. C., Karumuri, A.: Potential modulations of
612 pre-monsoon aerosols during El Niño: impact on Indian summer monsoon, *Clim. Dyn.*,
613 49(7-8), 2017.

614 Fadnavis, S., Müller, R., Kalita, G., Rowlinson, M., Rap, A., Li, J.-L. F., Gasparini, B., and
615 Laakso, A.: The impact of recent changes in Asian anthropogenic emissions of SO₂ on
616 sulfate loading in the upper troposphere and lower stratosphere and the associated
617 radiative changes, *Atmos. Chem. Phys.*, 19, 9989–10008, [https://doi.org/10.5194/acp-](https://doi.org/10.5194/acp-19-9989-2019)
618 19-9989-2019, 2019.

619 Fadnavis, S., Sabin, T. P., Rap, A., Müller, R., Kubin, A., and Heinold, B.: The impact of
620 COVID-19 lockdown measures on the Indian summer monsoon, *Environ. Res. Lett.* 16, 074054, <https://doi.org/10.1088/1748-9326/ac109c>, 2021a.

622 Fadnavis, S., Sioris, C. E., Wagh, N., Chattopadhyay, R., Tao, M., Chavan, P., Chakroborty,
623 T.: A rising trend of double tropopause s over South Asia in a warming environment:
624 Implications for moistening of the lower stratosphere, *Int. J. Climatol.*, 41, E200–E215,
625 DOI: 10.1002/joc.6677, 2021b.

626 Fisher, J., Jacob, A. D. J., Wang, Q., Bahreini, R., Carouge, C. C., Cubison, M. J. Dibb, J. E.
627 Diehl, T., Jimenez, J. L., Leibensperger, E. M., Lu, Z., Marcel, B., Havala, J. M., Pye,
628 O. T., Quinn, P. K., Sharma, S., Streets, D. G., Donkelaar, A., and Yantosca R. M.:
629 Sources, Distribution, and Acidity of Sulfate-Ammonium Aerosol in the Arctic in
630 Winter-Spring, *Atmos. Environ.*, 45(39):7301–18, 2011.

631 Gettelman, A. P., Piers, M., Fujiwara, M., Fu, Q., Vömel, H., Gohar, L. K., Johanson, C., and
632 Ammerman. M.: Radiation Balance of the Tropical Tropopause Layer, *J. Geophys. Res.:*
633 *Atmos.* 109(7):1–12, 2004.

634 Giglio, L., Descloitres, J. Justice, C. O. and Kaufman, Y. J.: An Enhanced Contextual Fire
635 Detection Algorithm for MODIS, *Remote Sens. of Environ.* 87(2–3):273–282, 2003.

636 Giglio, L.: MODIS Collection 6 Active Fire Product User’s Guide Revision A. Unpublished
637 Manuscript, Department of Geographical Sciences, University of Maryland.(
638 http://modisfire.umd.edu/files/MODIS_C6_Fire_User_Guide_A.pdf) March, 2015.

639 Guenther, A.: A Global Model of Natural Volatile Organic Compound Emissions, *J. Geophys.*
640 *Res.* 100(D5):8873–92, 1995.

641 Guha, A., Kumar, B., Dhar, D. P., Banik, T., Chakraborty, M., Roy, R., Choudhury, A.,
642 Mukunda, M., Gogoi, S., Babu, S., and Krishna Moorthy, K.: Seasonal Characteristics of
643 Aerosol Black Carbon in Relation to Long Range Transport over Tripura in Northeast
644 India, *Aerosol Air Qual. Res.* 15(3):786–98, 2015.

645 Guhathakurta, P., and Rajeevan, M.: Trends in the Rainfall Pattern over India, *Int. J.*
646 *Climatol.* 28(11):1453–69, 2008.

647 Hooghiem, J., Maria J. D., Popa, E., Thomas., R, Grooß, J-U. Tritscher, I., Müller, R., Kivi,
648 R., and Chen, H.: Wildfire Smoke in the Lower Stratosphere Identified by in Situ CO
649 Observations, *Atmos. Chem. and Phys.*, 20 (22): 13985–3. [https://doi.org/10.5194/acp-](https://doi.org/10.5194/acp-20-13985-2020)
650 [20-13985-2020](https://doi.org/10.5194/acp-20-13985-2020), 2020.

651 Hanumanthu, S., Vogel, B., Müller, R., Brunamonti, S., Fadnavis, S., Li, D., Ölsner, P., Naja,
652 M., Singh, B. B., Ravi Kumar, K., Sonbawne, S., Jauhiainen, H., Vömel, H., Luo, B.,
653 Jorge, T., Wienhold, F. G., Dirksen, R., and Peter, T.: Strong day-to-day variability of the
654 Asian Tropopause Aerosol Layer (ATAL) in August 2016 at the Himalayan foothills,
655 *Atmos. Chem. Phys.*, 20, 14273–14302, 2020, [https://doi.org/10.5194/acp-20-14273-](https://doi.org/10.5194/acp-20-14273-2020)
656 [2020](https://doi.org/10.5194/acp-20-14273-2020).

657 Khaykin, S. B., Legras, S., Bucci, P., Sellitto, L., Isaksen, F., Tencé, S., Bekki, A., Rieger, B.
658 L., Zawada, D., Jumelet, J., and Godin-Beekmann, S.: The 2019/20 Australian Wildfires

659 Generated a Persistent Smoke-Charged Vortex Rising up to 35 Km Altitude, *Commu.*
660 *Earth Environ.*, 1, 22. <https://doi.org/10.1038/s43247-020-00022-5>, 2020.

661 Lamarque, J. T., Bond, V., Eyring, C., Granier, A., Heil, Z., Klimont, D., Lee, C., Lioussé, A.,
662 Mieville, B., Owen, M., G., Schultz, D., Shindell, S., J., Smith, E., Stehfest, J., Van
663 Aardenne, O., R., Cooper, M., Kainuma, Mahowald, N., McConnell, J. R., Naik, V.,
664 Riahi, K., and Vuuren, D.: Historical (1850-2000) Gridded Anthropogenic and Biomass
665 Burning Emissions of Reactive Gases and Aerosols: Methodology and Application,
666 *Atmos. Chem. Phys.*, 10(15):7017–39, 2010.

667 Lau, W., Kim, M.-k., & Kim, K.: Asian summer monsoon anomalies induced by aerosol direct
668 forcing: The role of the Tibetan Plateau, *Clim. Dyn.*, 26, 855-864. [10.1007/s00382-006-](https://doi.org/10.1007/s00382-006-0114-z)
669 [0114-z](https://doi.org/10.1007/s00382-006-0114-z), 2006.

670 Lestrelin, H., Legras, B., Podglajen, A., and Salihoglu, M.: Smoke-charged vortices in the
671 stratosphere generated by wildfires and their behaviour in both hemispheres: comparing
672 Australia 2020 to Canada 2017, *Atmos. Chem. Phys.*, 21, 7113–7134,
673 <https://doi.org/10.5194/acp-21-7113-2021>, 2021.

674 Lin, C., Zhao, Y. C., Liu, X., Lin, N. H., and Chen, W. N.: Modelling of Long-Range
675 Transport of Southeast Asia Biomass-Burning Aerosols to Taiwan and Their Radiative
676 Forcings over East Asia. *Tellus, Series B: Chem. Phys. Meteorol.*, 66(1), 23733, 2014.

677 Li, Z., Yang, S., He, B., and Hu, C.: Intensified Springtime Deep Convection over the South
678 China Sea and the Philippine Sea Dries Southern China, *Sci. Rep.*, 6, 30470, 2016.

679 Matson, M., and J., Dozier.: Identification of Subresolution High Temperature Sources Using
680 a Thermal IR Sensor. *Photogramm. Eng. Remote Sensing*, 47(9), 1311–18, 1981.

681 [Maycock A. C., Joshi, M. M., Shine, K. P., Scaife, A. A.: The Circulation Response to](#)
682 [Idealized Changes in Stratospheric Water Vapor, *J. Clim.*, 26, 545-561, DOI:](#)
683 [10.1175/JCLI-D-12-00155.1, 2013.](#)

684 Meehl, G. A., Arblaster, J., and Collins, W. D.: Effects of Black Carbon Aerosols on the
685 Indian Monsoon, *J. Clim.*, 21(12),2869–82, 2008.

686 Mhawish, A. T., Banerjee, M., Sorek-Hamer, A., Lyapustin, D., Broday, and Chatfield, R.:
687 Comparison and Evaluation of MODIS Multi-Angle Implementation of Atmospheric
688 Correction (MAIAC) Aerosol Product over South Asia, *Remote Sens. of Environ.*, 224,
689 12–28, 2019.

690 Mieville, A., Granier, C., Liousse, C., Guillaume, B., Mouillot, F., Lamarque, J. F., Grégoire,
691 J. M., and Pétron, G.: Emissions of Gases and Particles from Biomass Burning during
692 the 20th Century Using Satellite Data and an Historical Reconstruction, *Atmos.*
693 *Environ.*, 44(11), 1469–77, 2010.

694 Murugavel, P., Pawar, S. D., and Gopalakrishnan, V. : Trends of Convective Available
695 Potential Energy over the Indian Region and Its Effect on Rainfall, *Int. J. Climatol.*,
696 32(9), 1362–72, 2012.

697 Nguyen, H. N., Bengt, G., Martinsson, J. B., Wagner, E., Carlemalm, M., Ebert, S.,
698 Weinbruch, C., Brenninkmeijer, A. M., Heintzenberg, J., Hermann, M., Schuck, T., van
699 Velthoven, P. F. J., and Zahn, A.: Chemical Composition and Morphology of Individual
700 Aerosol Particles from a CARIBIC Flight at 10 Km Altitude between 50°N and 30°S, *J.*
701 *Geophys. Res. Atmos.*, 113(23), 1–12, 2008.

702 Ni, H., Huang, R-J, Cao, J., Guo, J., Deng, H, and Dusek, U.: Sources and formation of
703 carbonaceous aerosols in Xi'an, China: primary emissions and secondary formation
704 constrained by radiocarbon, *Atmos. Chem. Phys.*, 19, 15609–15628,
705 <https://doi.org/10.5194/acp-19-15609-2019>, 2019.

706 Oman, L., D., Waugh, S., Pawson, R. S., Stolarski, and Nielsen, J. E.: Understanding the
707 Changes of Stratospheric Water Vapor in Coupled Chemistry-Climate Model
708 Simulations, *J. Atmos. Sci.*, 65(10), 3278–91, 2008.

709 Oshima, N., Kondo, Y., Moteki, N., Takegawa, N., Koike, M., Kita, K., Matsui, H., Kajino,
710 M., Nakamura, H., Jung, J. S., and Kim, Y. J.: Wet Removal of Black Carbon in Asian
711 Outflow: Aerosol Radiative Forcing in East Asia (A-FORCE) Aircraft Campaign, *J.*
712 *Geophys. Res. Atmos.*, 117(3), 1–24, 2012.

713 Peterson, D. A., Campbell J. R., Edward, J. H., Michael, D. F., George, P. K., Cossuth, J. H.,
714 and Matthew, T. D.: Wildfire-Driven Thunderstorms Cause a Volcano-like Stratospheric
715 Injection of Smoke, *Npj Clim. Atmos. Sci.*, 1(1), 1–8, 2018.

721 [Pozzoli, L., Bey I., Rast, S., Schultz, M. G. Stier, P., and Feichter, J.: Trace gas and aerosol](#)
722 [interactions in the fully coupled model of aerosol-chemistry-climate ECHAM5-](#)
723 [HAMMOZ: 1. Model description and insights from the spring 2001 TRACE-](#)
724 [Pexperiment, *J. Geophys. Res.*, 113, D07308, doi:10.1029/2007JD009007, 2018.](#)

725 Randel, W. J., Park, M., Emmons, L., Kinnison, D., Bernath, P., Walker, K. A., Boone, C.,
726 and Pumphrey H.: Asian Monsoon Transport of Pollution to the Stratosphere, *Sci.*,
727 328(5978), 611–13, 2010.

728 Rieger, L. A., Malinina, E. P., Rozanov V., Burrows J. P., Bourassa A. E., and Degenstein D.
729 A.: A study of the approaches used to retrieve aerosol extinction, as applied to limb
730 observations made by OSIRIS and SCIAMACHY, *Atmos. Meas. Tech.*, 11, 3433–3445,
731 <https://doi.org/10.5194/amt-11-3433-2018>, 2018.

732 Riese, M., Ploeger, F., Rap, A., Vogel, B., Konopka, P., Dameris, M., and Forster, P.: Impact
733 of uncertainties in atmospheric mixing on simulated UTLS composition and related
734 radiative effects, *J. Geophys. Res.*, 117, D16305, doi:10.1029/2012JD017751, 2012.

735 Schill, G. P., Froyd, K. D., Bian, H., Kupc, A., Williamson, C., Brock, C. A., Ray, E.,
736 Hornbrook, R. S., Hills, A. J., Apel, E. C., Chin, M., Colarco, P. R., and Murphy, D. M.:
737 Widespread Biomass Burning Smoke throughout the Remote Troposphere, *Nat. Geosci.*,
738 13(6), 422–27, 2020.

739 Schultz, M. G., Heil, A., Hoelzemann, J. J., Spessa, A., Thonicke, K., Goldammer, J. G.,
740 Alexander, C. H., Pereira, J. M. C., and Bolscher, M.: Global Wildland Fire Emissions
741 from 1960 to 2000, *Global Biogeochem. Cycles*, 22(2), 1–17, 2008.

742 Sherwood, S., Dixit, V., and Salomez, C.: The Global Warming Potential of Near-Surface
743 Emitted Water Vapour, *Environ. Res. Lett.*, 13(10), 104006, 2018.

744 Shindell, D., Chin, T. M., Dentener, F., Doherty, R. M., Faluvegi, G., Fiore, A. M., Hess, P.,
745 Koch, D. M., MacKenzie, I. A., Sanderson, M. G., Schultz, M. G., Schulz, M.,
746 Stevenson, D. S., Teich, H., Textor, C., Wild, O., Bergmann, D., J., Bey, I., Bian, H.,
747 Cuvelier, C., Duncan, B. N., Folberth, G., Horowitz, L. W., Jonson, J., Kaminski, J. W.,
748 Marmer, E., Park R., Pringle, K. J., Schroeder, S., Szopa, S., Takemura, T., Zeng, G.,
749 Keating, T. J., and Zuber. A.: A Multi-Model Assessment of Pollution Transport to the
750 Arctic, *Atmos. Chem. Phys.*, 8(17), 5353–72, 2008.

751 Singh, N., Murari, V., Kumar, M., Barman, S. C., and Banerjee, T.: Fine Particulates over
752 South Asia: Review and Meta-Analysis of PM_{2.5} Source Apportionment through
753 Receptor Model, *Environ. Pollut.*, 223, 121–136, 2017.

754 Singh, P., Sarawade, P., and Adhikary, B.: Transport of Black Carbon from Planetary
755 Boundary Layer to Free Troposphere during the Summer Monsoon over South Asia.
756 *Atmos. Res.*, 235, 104761, 2020.

757 Singh, P., Sarawade, P., and Adhikary, B.: Carbonaceous Aerosol from Open Burning and Its
758 Impact on Regional Weather in South Asia, *Aerosol Air Qual. Res.*, 20(3), 419–31, 2020.

759 Stier, P., Feichter, J., Kinne, S., Kloster, S., Vignati, E., Wilson, J., Ganzeveld, L.: The
760 Aerosol-Climate Model ECHAM5-HAM, *Atmos. Chem. Phys.*, 5(4), 1125–1156,
761 <https://doi.org/10.5194/acp-5-1125-2005>, 2005.

762 Streets, D. G., Yarber, K. F., Woo, J. H., and Carmichael, G. R.: Biomass Burning in Asia:
763 Annual and Seasonal Estimates and Atmospheric Emissions, *Global Biogeochem.*

764 Cycles, 17(4), 1099, doi:10.1029/2003GB002040, 2003.

765 Talukdar, S., Jana, S., Maitra, A., and Gogoi, M. M. : Characteristics of Black Carbon
766 Concentration at a Metropolitan City Located near Land-Ocean Boundary in Eastern
767 India, *Atmos. Res.*, 153, 526–34, 2015.

768 Tegen, I., Neubauer, D., Ferrachat, S., Drian, C., Bey, I., Schutgens, N., Stier, P., Duncan, W.
769 P., Stanelle, T., Schmidt, H., Rast, S., Kokkola, H., Schultz, M., Sabine, S., Daskalakis,
770 N., Barthel, S., Heinold, B., and Lohmann, U.: The Global Aerosol-Climate Model
771 Echem6.3-Ham2.3 -Part 1: Aerosol Evaluation, *Geosci. Model Dev.*, 12(4), 1643–77,
772 2019.

773 [Textor, C., Schulz, M., Guibert, S., Kinne, S., Balkanski, Y., Bauer, S., Berntsen, T.,
774 Berglen, T., Boucher, O., Chin, M., Dentener, F., Diehl, T., Easter, R., Feichter, H.,
775 Fillmore, D., Ghan, S., Ginoux, P., Gong, S., Grini, A., Hendricks, J., Horowitz, L.,
776 Huang P. Isaksen I., Iversen, I., Kloster, S., Koch, D., Kirkevåg, A., Kristjansson, J.
777 E., Krol, M., Lauer, A. Lamarque, J. F., Liu, X., Montanaro, V., Myhre, G., Penner,
778 J., Pitari, G., Reddy, S., Seland, Ø., Stier, P., Takemura, T., and Tie, X.: Analysis and
779 quantification of the diversities of aerosol life cycles within AeroCom, *Atmos. Chem.
780 Phys.*, 6, 1777–1813, 2006, <https://doi.org/10.5194/acp-6-1777-2006>.](#)

781 Thomas, A., Sarangi, C., and Kanawade, V. P.: Recent Increase in Winter Hazy Days over
782 Central India and the Arabian Sea, *Sci. Rep.*, 9(1), 1–10, 2019.

783 Val Martin, M., Logan, J. A., Kahn, R. A., Leung, F.-Y., Nelson, D. L., and Diner, D. J.:
784 Smoke injection heights from fires in North America: analysis of 5 years of satellite
785 observations, *Atmos. Chem. Phys.*, 10, 1491–1510, [https://doi.org/10.5194/acp-10-1491-](https://doi.org/10.5194/acp-10-1491-2010)
786 2010, 2010.

787 Van Der Werf, G. R., Randerson, J. T., Giglio, L., Collatz, G. J., Kasibhatla, P. S., and
788 Arellano, A. F.: Interannual Variability in Global Biomass Burning Emissions from 1997

789 to 2004, *Atmos. Chem. and Phys.*, 6(11), 3423–41, 2006.

790 Wang, S. H., Lin, N. H., Chou, M. D., and Woo. J. H.: Estimate of Radiative Forcing of Asian
791 Biomass-Burning Aerosols during the Period of TRACE-P, *J. Geophys. Res. Atmos.*,
792 112(10), 1–17, 2007.

793 Wang, S. H., Ellsworth, J. W., Holben, B. N., Tsay S. C., Lin, N. H., Giles, D., Sebastian, A.
794 S., Xuan, S. J., Nguyen, A., Hsiao, T., Chen, W. N., Lin, T. H., Buntoung, S. S. C., and
795 Wiriya. W.: Vertical Distribution and Columnar Optical Properties of Springtime
796 Biomass- Burning Aerosols over Northern Indochina during 2014 7-SEAS Campaign,
797 *Aerosol Air Qual. Res.*, 15(5), 2037–50, 2015.

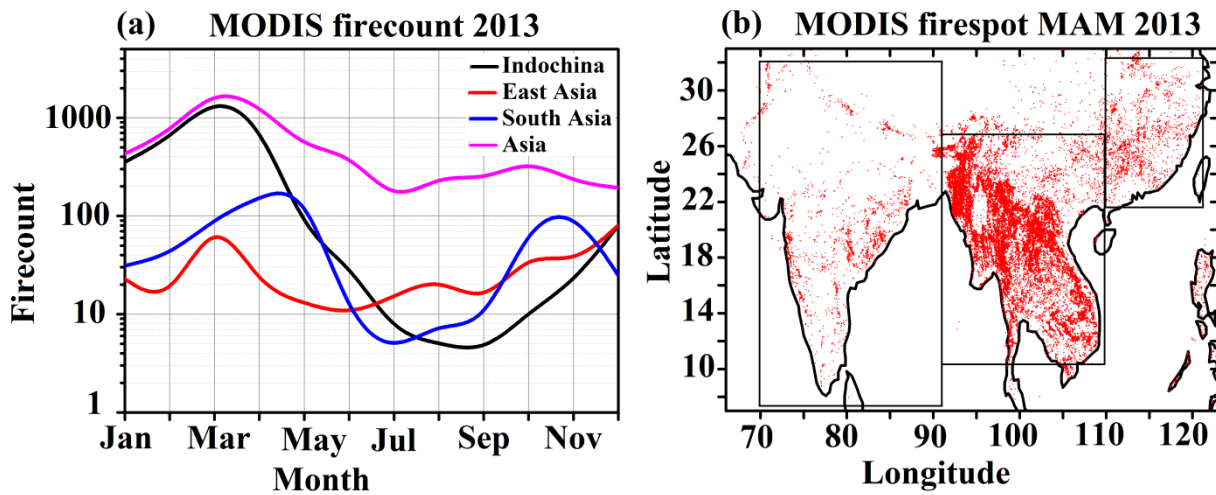
798 Weigel, R., Mahnke, C., Baumgartner, M., Dragoneas, A., Vogel, B., Ploeger, F., Viciani, S.,
799 D'Amato, F., Bucci, S., Legras, B., Luo, B., and Borrmann, S.: In situ observation of
800 new particle formation (NPF) in the upper troposphere/lower stratosphere of the 2017
801 Asian monsoon anticyclone, Part 1: Summary of StratoClim results, *Atmos. Chem.*
802 *Phys.*, <https://doi.org/10.5194/acp-21-11689-2021>, 2021.

803 Wu, J., Kong, S., Wu, F., Cheng, Y., Zheng, S., Yan, Q., Zheng, H., Yang, G., Zheng, M., Liu,
804 D., Zhao, D., and Qi, S.: Estimating the Open Biomass Burning Emissions in Central
805 and Eastern China from 2003 to 2015 Based on Satellite Observation, *Atmos. Chem.*
806 *Phys.*, 18(16), 11623–46, 2018.

807 Xie, F., Tian, W., Zhou, X., Zhang, J., Xia, Y., and Lu, J.: Increase in Lower Stratospheric
808 Water Vapor in the Past 100 Years Related to Tropical Atlantic Warming, *Geophys. Res.*
809 *Lett.*, 47, e2020GL090539. <https://doi.org/10.1029/2020GL090539>, 2020.

810 Zhang, X., Liu, J., Han, H., Zhang, Y., Jiang, Z., Wang, H., Meng, L., Li, Y. C., and Liu Y.:
811 Satellite-Observed Variations and Trends in Carbon Monoxide over Asia and Their
812 Sensitivities to Biomass Burning, *Remote Sens.* 12(5), 2020.

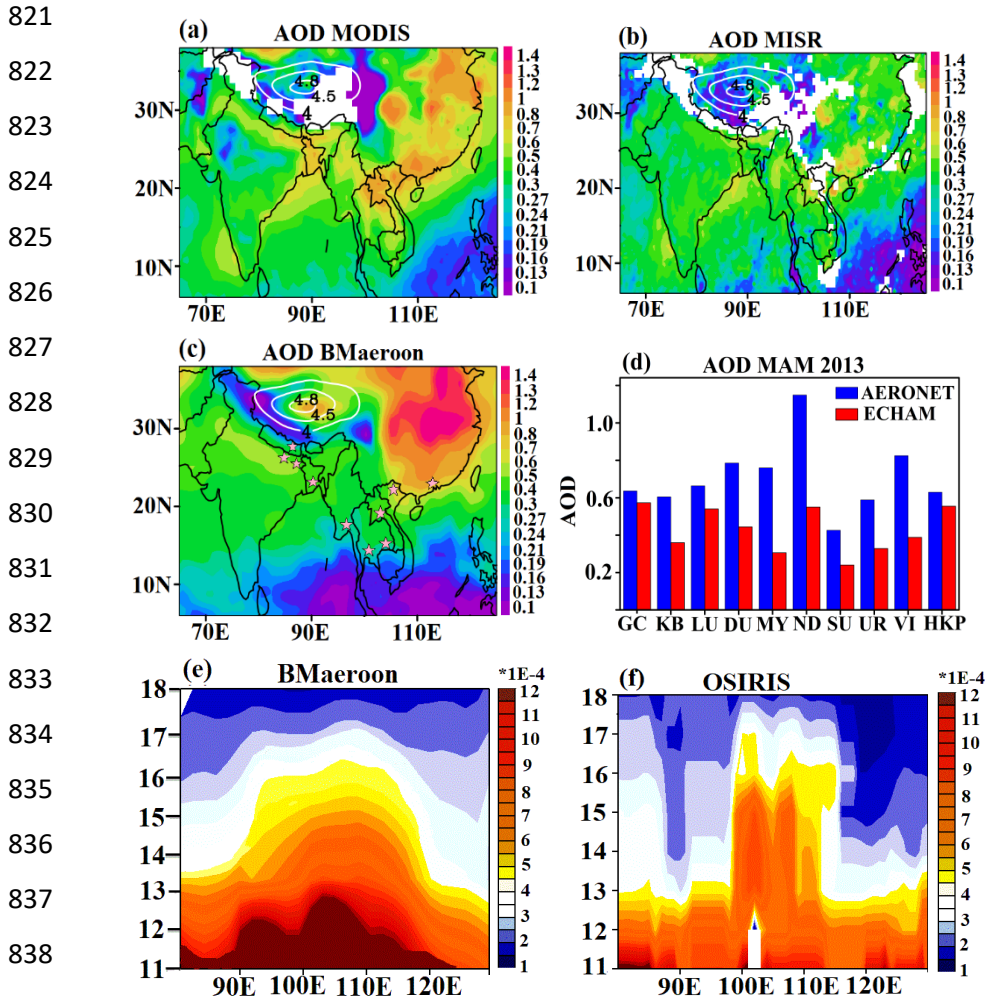
813



814

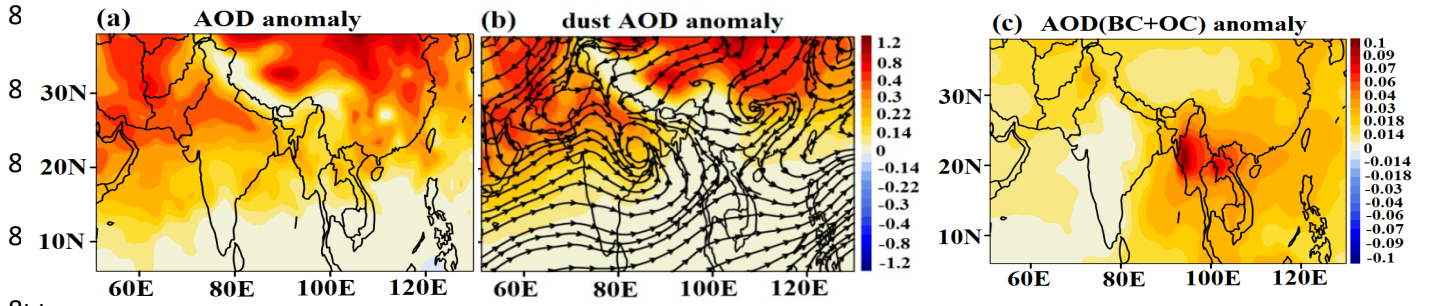
815 **Figure 1:** (a) Monthly mean distribution of MODIS fire counts averaged over Indochina
 816 (91°E - 107°E, 10°N - 27°N), East Asia (108°E - 123°E, 22°N - 32°N), South Asia (70°E -
 817 90°E, 8°N - 32°N) and Asia (60°E - 130°E, 10°S - 50°N) (b) Spatial distribution of fire spots
 818 over South Asia, Indochina and East Asia averaged for spring 2013. Boxes in Figure (b)
 819 indicate the boundaries of South Asia, Indochina, and East Asia.

820



839 **Figure 2:** (a) Aerosol optical depth (AOD) averaged for spring 2013 from MODIS, (b) same
 840 as (a) but from MISR, (c) same as (a) but from ECHAM6 - HAMMOZ BMAeroon
 841 simulation. **White contours in Fig (a)-(c) indicate the orography (km) of the Tibetan Plateau,**
 842 (d) Comparison of simulated AOD (from BMAeroon) averaged for spring 2013 with
 843 AERONET observations at Gandhi college (GC; 25.81°N - 85.12°E), Kathmandu Bode (BD;
 844 27.68°N - 85.39°E), Lumbini (LU; 27.49°N - 83.28°E), Dhaka University (DU; 23.72°N -
 845 90.39°E), Myanmar(MY; 16.86°N-96.15°E), Nghia Do (ND; 21.04°N - 105.80°E), Silpakorn
 846 University (SU; 13.81°N - 100.04°E), Ubon Ratchathani (UR; 15.24°N - 104.87°E),
 847 Vientiane (VI; 17.99°N - 102.57°E), Hong Kong Poly (HKP; 22.30°N – 114.18°E). (e)
 848 Simulated (BMAeroon) aerosol extinction coefficient (865 nm) (km^{-1}), averaged for 12°N -
 849 30°N and spring 2013 (f) same as (e) but from OSIRIS measurements (750 nm).

850



855

856

857 **Figure 3:** Distribution of ECHAM6-HAMMOZ simulated anomalies of (BMaeroon -
858 BMaerooff) (a) AOD, (b) dust AOD, (c) BC-AOD and OC-AOD, together, averaged for
859 spring 2013. Streamlines in figure 3b indicate wind anomalies at 900 hPa (BMaeroon-
860 BMaerooff).

861

862

863

864

865

866

867

868

869

870

871

872

873

874

875

876

877

878

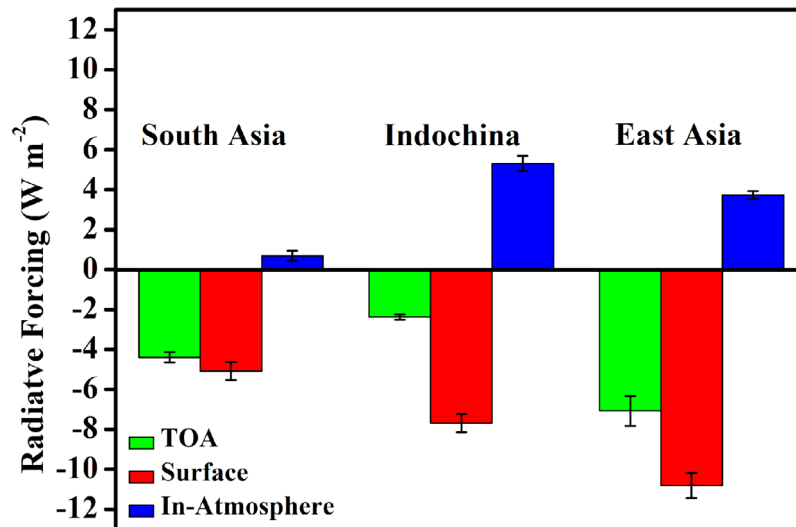
879

880

881

882

883

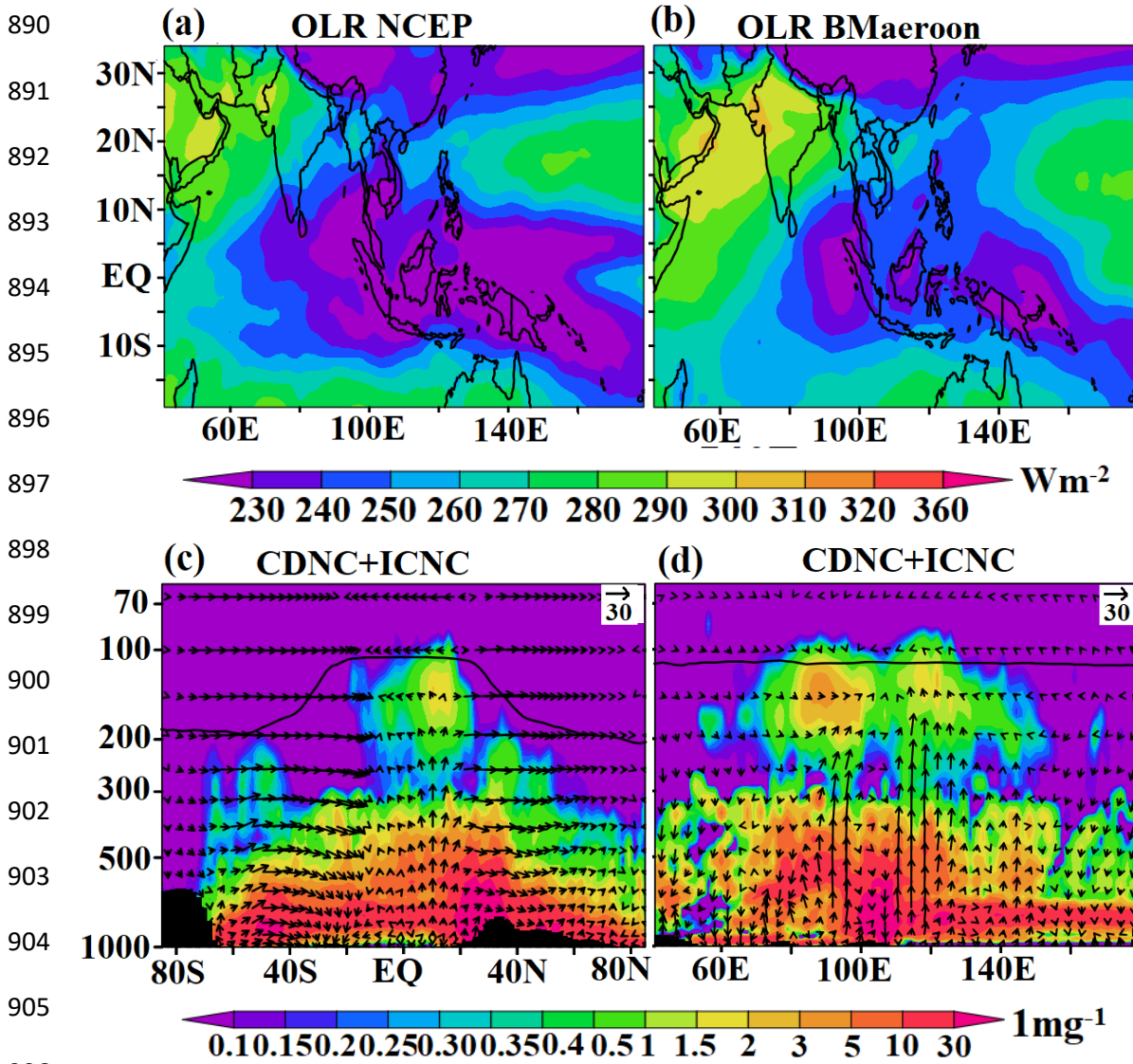


884

885 **Figure 4:** Anomalies of radiative forcing ($\text{W}\cdot\text{m}^{-2}$) from ECHAM6-HAMMOZ simulations
886 (BMaeroon - BMaerooff) at the TOA, surface, and in-atmosphere (TOA - Surface) averaged
887 for spring 2013 and over South Asia, Indochina, and East Asia.

888

889



907 **Figure 5:** (a) Distribution of Outgoing Longwave Radiation (OLR) ($W m^{-2}$) from NCEP
 908 reanalysis-2 data averaged for spring 2013, (b) same as (a) but from the ECHAM6-
 909 HAMMOZ simulations (BMaeroon). Vertical distribution of cloud droplet number
 910 concentration (CDNC) and ice crystal number concentration (ICNC) ($1 mg^{-1}$) averaged for
 911 spring 2013 from ECHAM6-HAMMOZ simulations (BMaeroon) (c) latitude-pressure section
 912 (average for $85^{\circ}E-140^{\circ}E$) and (d) longitude-pressure section (average for $10^{\circ}N - 20^{\circ}N$).
 913 Vectors of the circulation (BMaeroon) are shown in (c)-(d) with the vertical velocity field
 914 scaled by 300.

915
 916

917

918

919

920

921

922

923

924

925

926

927

928

929

930

931

932

933

934

935

936

937

938

939

940

941

942

943

944

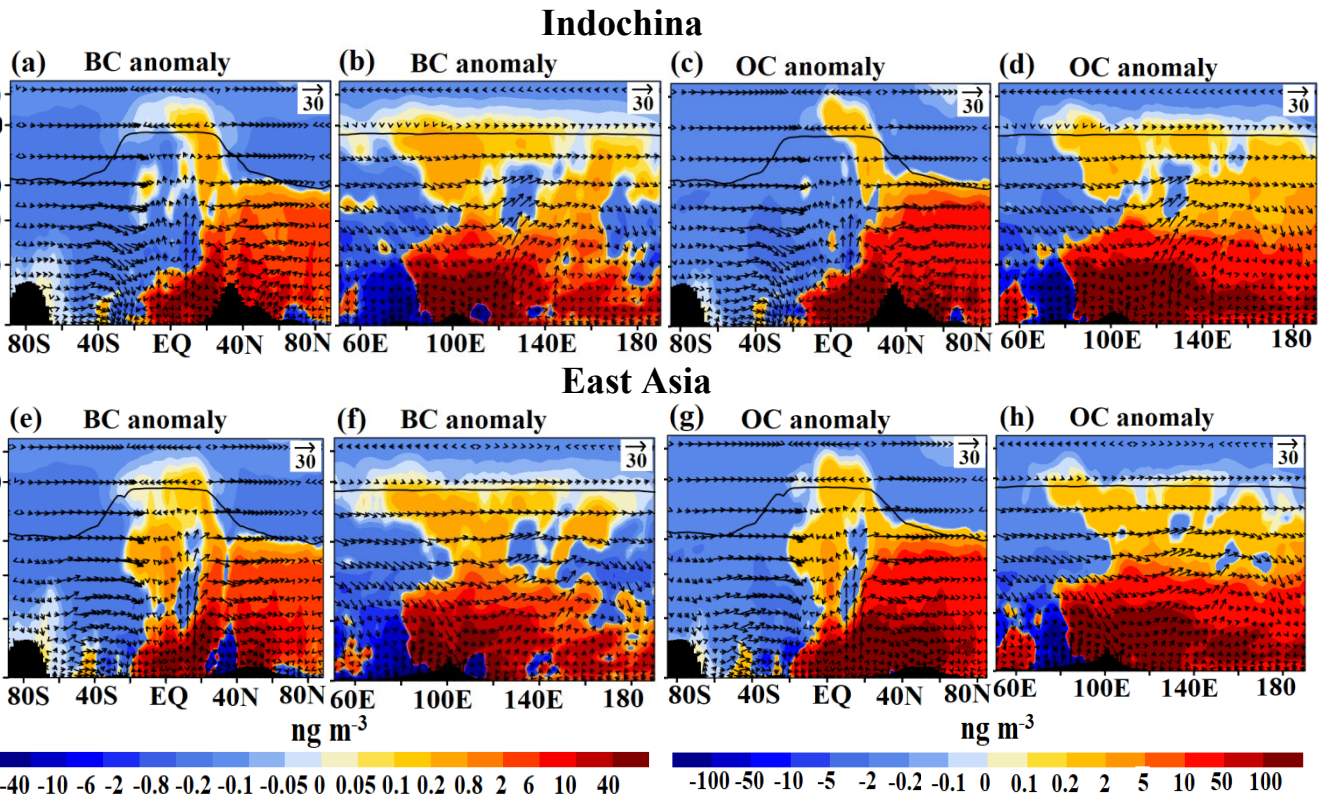


Figure 6: Vertical cross-section of anomalies of BC (ng m^{-3}) (BMaeroon – Bmaerooff) averaged for spring 2013 (a) latitude-pressure section (averaged for 91°E - 107°E), (b) longitude-pressure section (averaged for 18°N - 24°N). (c-d) is the same as (a-b) but for OC. (e) same as (a) but averaged over 108°E - 123°E , (f) same as (b) but averaged for 18°N - 24°N . (g-h) same as in (e-f) but for OC. The arrows in (a-h) indicate winds in m s^{-1} with the vertical velocity field scaled by 300. The black vertical bars show the topography and the black line indicates the tropopause.

945
946
947
948
949
950
951
952
953
954
955
956
957
958
959
960
961
962
963
964
965
966
967
968
969
970
971

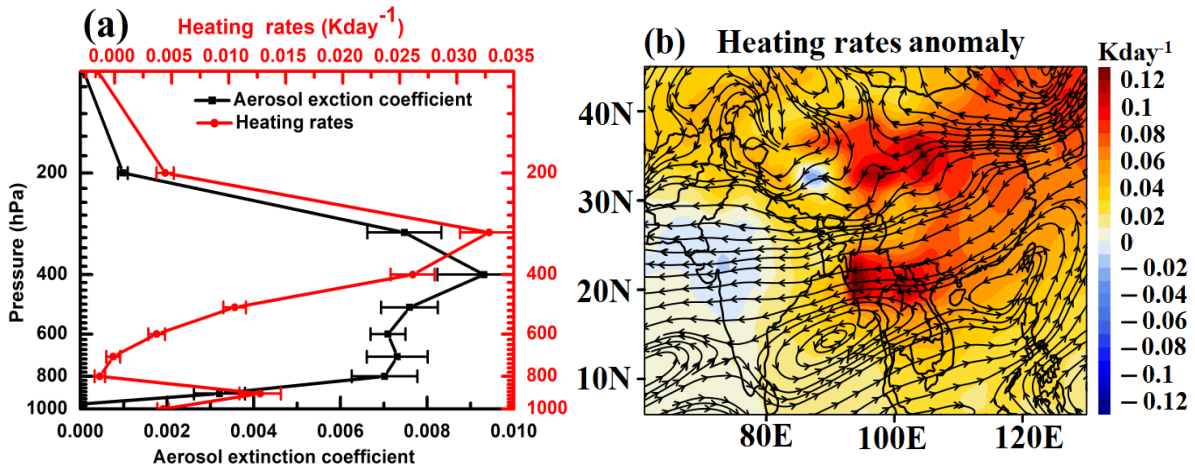


Figure 7: (a) Vertical profile of anomalies of extinction (km⁻¹) and heating rate (K day⁻¹) over the Arctic region (65°N-85°N) from the ECHAM6-HAMMOZ simulations (BMAeroon - BMAerooff). The horizontal lines indicate the standard deviation within the 10 members of the different initial conditions, (b) spatial distribution of anomalies of heating rates (K.day⁻¹) (short and long wave together) averaged from the surface to the tropopause. Streamlines in (b) indicate wind anomalies at 500 hPa (BMAeroon- BMAerooff).

972

973

974

Indochina

975

(a) Heating rate anomaly

(b) Heating rate anomaly

976

977

978

979

980

981

982

983

984

985

986

987

988

989

East Asia

(c) Heating rate anomaly

(d) Heating rate anomaly

990

991

992

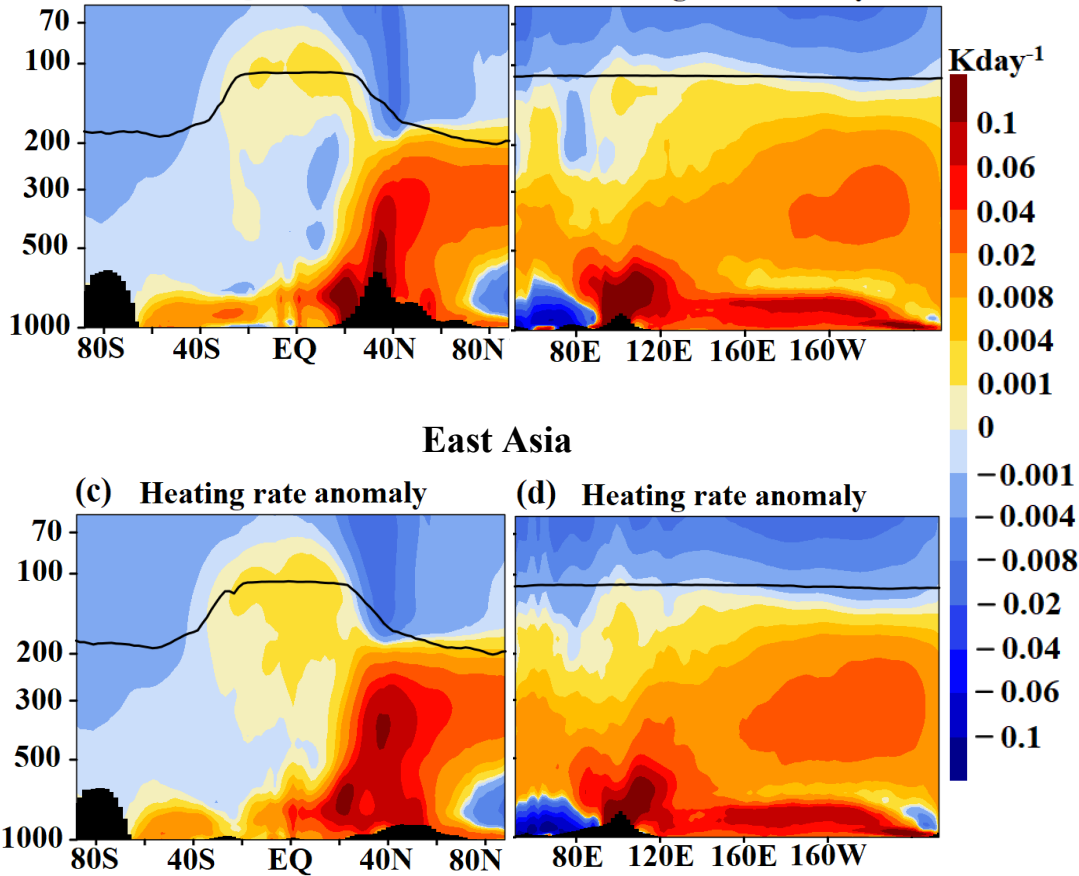
993

994

995

996

997



990 **Figure 8:** Vertical section of heating rate anomalies (K day^{-1}) for spring season 2013 from
991 ECHAM6-HAMMOZ simulations (BMaeroon - BMaerooff) (a) latitude-pressure section
992 averaged for 91°E - 107°E , (b) longitude-pressure section averaged for 18°N - 24°N . (c) same as
993 (a) but averaged for 108°E - 123°E . (d) same as (b) but averaged for 22°N - 27°N . The black
994 vertical bars show the topography and the black line indicates the tropopause.

995

996

997

998
999
1000
1001
1002
1003
1004
1005
1006
1007
1008
1009
1010
1011
1012
1013
1014
1015
1016
1017
1018
1019
1020
1021
1022
1023

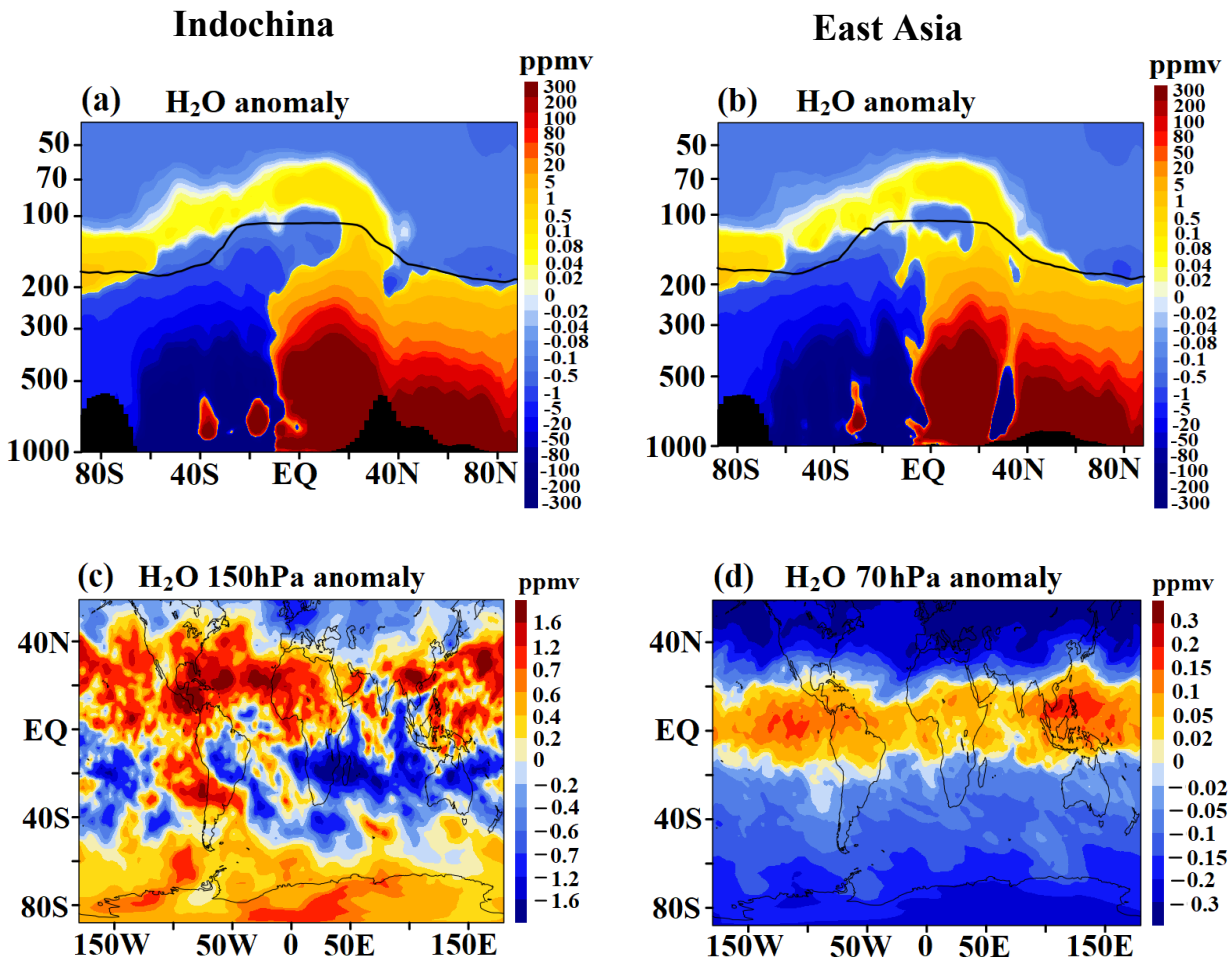


Figure 9: Vertical and horizontal distribution of anomalies of water vapour (ppmv) for spring 2013 from the ECHAM6-HAMMOZ simulations (BMAeroon - BMAerooff) (a) latitude-pressure cross-section averaged for 91°E-107°E, (b) longitude-pressure cross-section averaged over 108°E-123°E, at (c) 150 hPa level, and (d) 70 hPa level. In Fig (a)-(b) the black vertical bars show the topography and the black line indicates the tropopause.